Optomechanical Tuning of Second Harmonic Generation Anisotropy in Janus MoSSe/MoS_2 Heterostructures

Kunyan Zhang[1,2,*], Medha Dandu[3,4], Nguyen T. Hung[5,6], Tianyi Zhang[7], Elyse Barré[3], Riichiro Saito[5,8], Jing Kong[7], Archana Raja[3,9], Shengxi Huang[10,*]

[1]Department of Chemistry, University of California, Berkeley, Berkeley, California 94720, USA

[2]Molecular Biophysics and Integrated Bioimaging Division, Lawrence Berkeley National Laboratory, Berkeley, California 94720, USA

[3]Molecular Foundry, Lawrence Berkeley National Laboratory, Berkeley, California 94720, USA

[4]Chemistry and Physics of Materials Unit, Jawaharlal Nehru Centre for Advanced Scientific Research, Bengaluru, 560064, India

[5]Department of Physics, Tohoku University, Sendai 980-8578, Japan

[6]Department of Materials Science and Engineering, National Taiwan University, Taipei, 10617, Taiwan

[7]Department of Electrical Engineering and Computer Science, Massachusetts Institute of Technology, Cambridge, Massachusetts 02139, USA

[8]Department of Physics, National Taiwan Normal University, Taipei, 11677, Taiwan

[9]Kavli Energy NanoScience Institute, University of California, Berkeley, Berkeley, CA 94720, USA

[10]Department of Electrical and Computer Engineering and the Rice Advanced Materials Institute, Rice University, Houston, Texas 77005, USA

*Corresponding author: Shengxi Huang (shengxi.huang@rice.edu), Kunyan Zhang (kunyanzhang@berkeley.edu)

Abstract

Symmetry breaking in van der Waals materials enables the realization of quantum states and advanced device functionalities. Janus transition metal dichalcogenides (TMDs) exhibit distinctive nonlinear optical properties due to their broken out-of-plane mirror symmetry. However, the dynamic control of SHG anisotropy and resonance behavior via optical excitation remains elusive. In this work, we investigate the SHG response of Janus MoSSe/MoS_2 heterostructures with 2H and 3R stackings. We can tune the SHG response by varying the incident photon wavelength from 800 nm to 1000 nm, which shows a resonance-dependent enhancement in intensity and a deviation from six-fold symmetry, indicating wavelength-dependent anisotropy. The ratio between maximum and minimum intensity in the armchair directions, associated with the SHG anisotropy, reaches a value of 1.73 at the excitation wavelength of 1000 nm. Group theory analysis and first-principles calculations reveal that the observed anisotropy arises from optically induced strain. Our findings highlight the role of symmetry breaking and optical resonance contributing to the optomechanical tuning of SHG anisotropy, offering opportunities for developing Janus TMD-based photonic devices for frequency conversion, light generation, and optical switching.

Keywords: Janus transition metal dichalcogenides, second harmonic generation, optical resonance, strain, optostriction, interlayer coupling.

Introduction

Symmetry breaking in layered van der Waals materials through stacking, sliding, and substitution gives rise to superior material properties that push the limit of practical applications.[1] Janus transition metal dichalcogenides (TMDs) are a type of two-dimensional (2D) material with broken out-of-plane mirror symmetry, in which the transitional metal is sandwiched between two different chalcogen species.[2-5] This asymmetric structure of Janus TMDs results in an inherent electric dipole moment, which leads to strong out-of-plane piezoelectricity,[2, 6] enhanced and tunable interlayer coupling,[7, 8] and large nonlinear susceptibility beyond conventional TMD materials.[9] Second harmonic generation (SHG) is a nonlinear optical process where the incident photon frequency (ω) is doubled (2ω) after passing through the non-centrosymmetric material (Figure 1a). For Janus TMDs, it has been demonstrated that 1T' MoSSe exhibits SHG intensities more than three times higher than 2H MoS_2.[9] While the SHG intensity vanishes in even numbers of conventional TMDs with 2H stacking due to the restored centrosymmetry, a bilayer Janus $MoSSe/MoS_2$ heterostructure with 2H stacking has a nonzero SHG susceptibility, which can be further tuned by uniaxial strain.[10] These characteristics showcase Janus TMD as an ideal platform to study the nonlinear optical properties of asymmetric van der Waals materials.

By exploring the wavelength and polarization dependence of SHG signals, we can gain valuable insights into the electronic band structure and symmetry properties of Janus TMDs.[11] For example, optical resonance can enhance the SHG signals in TMD heterostructures when an incident wavelength that matches the exciton transitions is employed.[12-15] Therefore, the wavelength dependence of SHG provides insight into the electronic band structure and enables the optimization of SHG efficiency for wavelength-specific nonlinear optics. Since the SHG intensity relies on symmetry breaking, the polarization dependence of SHG on the angle of the incident photon reveals the symmetry and orientation of the crystal lattice. In conventional TMDs, it has been demonstrated that the polarization dependence of SHG can be used to identify domain boundaries[16] and evaluate strains with high sensitivity.[17-19] While the enhanced interlayer coupling and strong electronic hybridization[7, 8] may offer tunability of optical nonlinearity, the dynamic control of SHG anisotropy in Janus TMD heterostructures via optical excitation remains elusive.

In this work, we investigate the SHG of Janus $MoSSe/MoS_2$ heterostructures with 2H and 3R stacking orders. The incident photon wavelength is tuned from 800 nm to 1000 nm, and the second-order nonlinear response is recorded from 400 nm to 500 nm, respectively. While the SHG intensity of monolayer MoSSe shows a near-perfect six-fold symmetry with respect to the polarization angles, the polarization dependence of SHG intensity in $MoSSe/MoS_2$

heterostructures deviates from the six-fold symmetry. The intensity ratio between the maximum and minimum SHG intensity in the armchair directions, which represents the level of anisotropy, becomes increasingly larger for longer laser wavelengths. Particularly, for MoSSe/MoS_2 with 2H stacking, the intensity ratio reaches the value of 1.73 at an excitation wavelength of 1000 nm. First-principles calculations predict the second-order susceptibility tensor as a function of incident wavelength due to resonance with excitons. We attribute the anisotropy to strain based on group theory analysis, where the strain is optomechanically induced by the electromagnetic field of incident light. This strain has only been achieved in Janus heterostructures because of the structural asymmetry that contributes to the strong interlayer coupling for strain transfer, whose extent varies between 3R and 2H stackings. Our work demonstrates the effect of crystal symmetry and optical resonance on the optomechanically tuning of SHG anisotropy in low-dimensional materials. Combined with their atomically thin nature, the anisotropic nonlinear optical response of Janus TMD heterostructures promises on-chip photonic applications, including frequency conversion, quantum light generation, optical switching, and sensing.

Results and Discussion

Second Harmonic Generation in 2H and 3R MoSSe/MoS_2

Janus MoSSe/MoS_2 heterostructures with 3R and 2H stackings (Figure 1b) were fabricated by plasma-assisted selenization of bilayer MoS_2 (Methods).[7, 20] In this process, the hydrogen radicals generated by plasma selectively bond to sulfur atoms in the topmost chalcogen layer, and then leave the surface as H_2S, while the sulfur layers underneath remain intact. Subsequently, the resulting sulfur vacancies are replaced with selenium atoms; hence, only the top layer of MoS_2 is converted into Janus MoSSe, and the stacking order and clean interface are preserved in the synthesized MoSSe/MoS_2 (Fig. S1). The bilayer 3R and 2H heterostructures and monolayer MoSSe can be identified in the optical images (Figure 1c-d). We performed polarization-dependent SHG measurements on the 3R and 2H MoSSe/MoS_2 by changing the angle of the incident laser with respect to the crystal axis. The SHG response polarized parallel to the incident beam was collected.

The polarization dependences of the SHG intensity under an 800 nm excitation exhibit a six-fold rotational symmetry for both stacking configurations (Figure 1e-f), MoS_2 (Fig. S2) and MoSSe (Fig. S3). The SHG polar plots can be fitted using $I_{\parallel} = \cos^2(3\phi - 3\varphi_0)$, in which $\phi - \varphi_0$ is the angle between the laser polarization and the armchair direction, and φ_0 is a constant that denotes the angle between the armchair direction of the crystal and the horizontal axis in the experimental geometry. Unlike 2H MoS_2 bilayers with vanishing SHG response, 2H MoSSe/MoS_2 exhibits a finite SHG intensity, about one-tenth of that in 3R MoSSe/MoS_2, suggesting broken centrosymmetry due to the atomic structure of MoSSe.

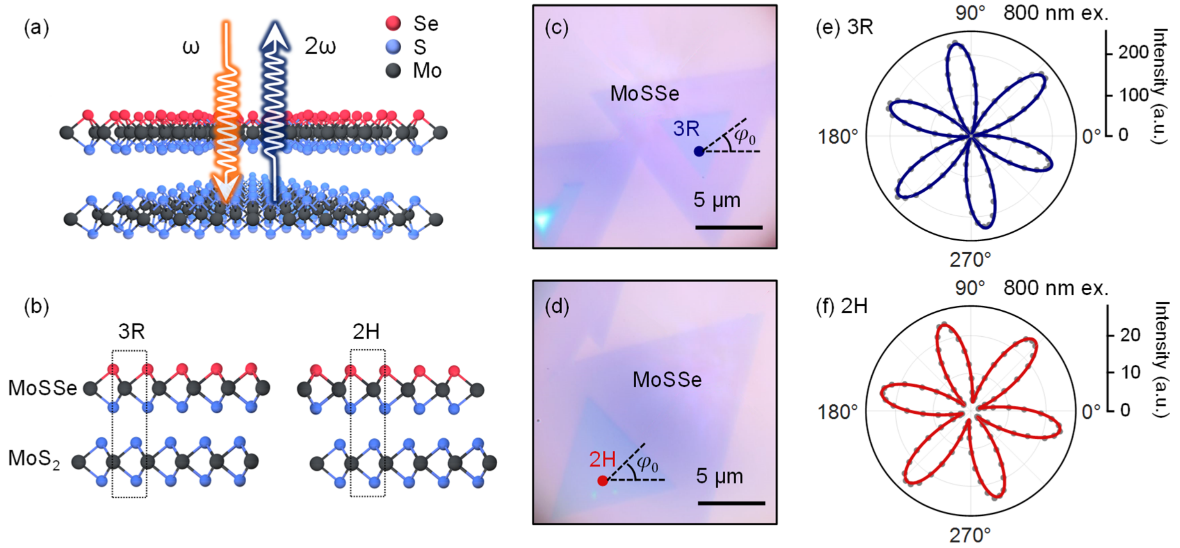

Figure 1. Second harmonic generation of Janus MoSSe/MoS_2. (a) Illustration of second harmonic generation of MoSSe/MoS_2. (b) Crystal structures of MoSSe/MoS_2 with 3R and 2H stackings. Optical images of (c) 3R and (d) 2H-stacked samples. SHG intensity of (e) 3R and (f) 2H MoSSe/MoS_2 as a function of polarization angle of the incident 800 nm laser. The 0 degree is along the *X*-axis of the experimental geometry.

Wavelength-Dependent Polarization-Resolved SHG

To investigate how excitation wavelength affects the SHG of monolayer MoSSe and Janus heterostructures, we measured the polarization dependence of SHG intensity under excitations ranging from 800 nm to 1000 nm in 25 nm steps. The detection range was set from 400 nm to 500 nm, corresponding to the second harmonic wavelengths. The average SHG intensities when the incident laser is polarized along the armchair directions are summarized in Figure 2 for different incident wavelengths. The SHG intensity of monolayer MoSSe (Figure 2a) increases as the incident wavelength shifts from 800 nm to 975 nm (1.55 eV to 1.27 eV), consistent with a previous study showing stronger SHG intensities at lower laser energies in MoSSe.[11] The SHG intensity reaches the maximum at 975 nm excitation (2.54 eV emission) for MoSSe and 3R MoSSe/MoS_2 and at 925 nm excitation for 2H MoSSe/MoS_2 (Figure 2c), which can be attributed to resonance with the transitions at the Γ point.[21, 22] The difference in the corresponding wavelength for 3R and 2H heterostructures may be explained by a slightly different energy gap at the Γ point.

We calculated the second-order susceptibility using first-principles calculations as shown in Figure 2d. The overall dependence of the calculated second-order susceptibility is qualitatively consistent with the experiments. Specifically, the calculated $\chi^{(2)}_{xxx}$ for the 3R heterostructure increases with increasing wavelength and eventually plateaus, while the calculated $\chi^{(2)}_{xxx}$ for 2H increases and then decreases, matching the experimental SHG intensity trend. The calculated spectrum is shifted to shorter wavelengths compared to the experiments, which can be attributed to the limited inclusion of many-body effects in the calculation, such as excitonic corrections.

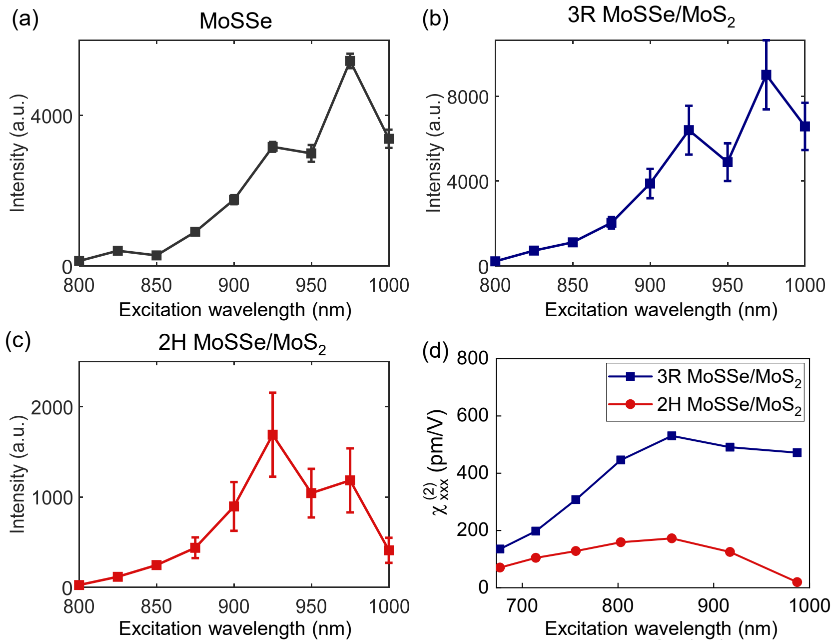

Figure 2. The fitted average SHG intensity for (a) MoSSe, (b) 3R MoSSe/MoS$_2$, and (c) 2H MoSSe/MoS$_2$ in the experiments. The squares denote the average SHG intensity along the six armchair directions. The error bars are the standard deviation of the SHG intensities along the six armchair directions. (d) The calculated second-order susceptibility tensor without strain as a function of incident wavelength.

Figure 3 presents representative polarization-dependent SHG intensities under 850, 900, 950, and 1000 nm excitations. The intensity polar plots of other excitation wavelengths are shown in Fig. S3–S6. The SHG of the MoSSe monolayer consistently shows a six-fold rotational symmetry for longer incident wavelengths, as shown in Figure 3, first row. However, the polarization dependence of the MoSSe/MoS$_2$ heterostructures deviates from the group theory prediction for the C_{3v} point group (Figure 3, second and third rows). For example, for 3R MoSSe/MoS$_2$ measured under 850 nm excitation, the SHG intensity for ϕ = 157° is slightly smaller than that for ϕ = 99°. This difference in SHG intensities along the three armchair directions becomes increasingly evident as the excitation wavelength becomes longer. Specifically, the SHG intensities of 3R MoSSe/MoS$_2$ under 1000 nm excitation for ϕ = 35° and 157° are both smaller than the SHG intensity for ϕ = 99°. Similar variations in SHG intensity are also observed in 2H MoSSe/MoS$_2$. While the SHG intensity of 2H MoSSe/MoS$_2$ is roughly the same for ϕ = 45° and 109° under 850 nm excitation, the SHG intensity for ϕ = 109° is approximately two times those at ϕ = 45° under 1000 nm excitation. This observation suggests an additional breaking of crystal symmetry that alters the SHG responses.

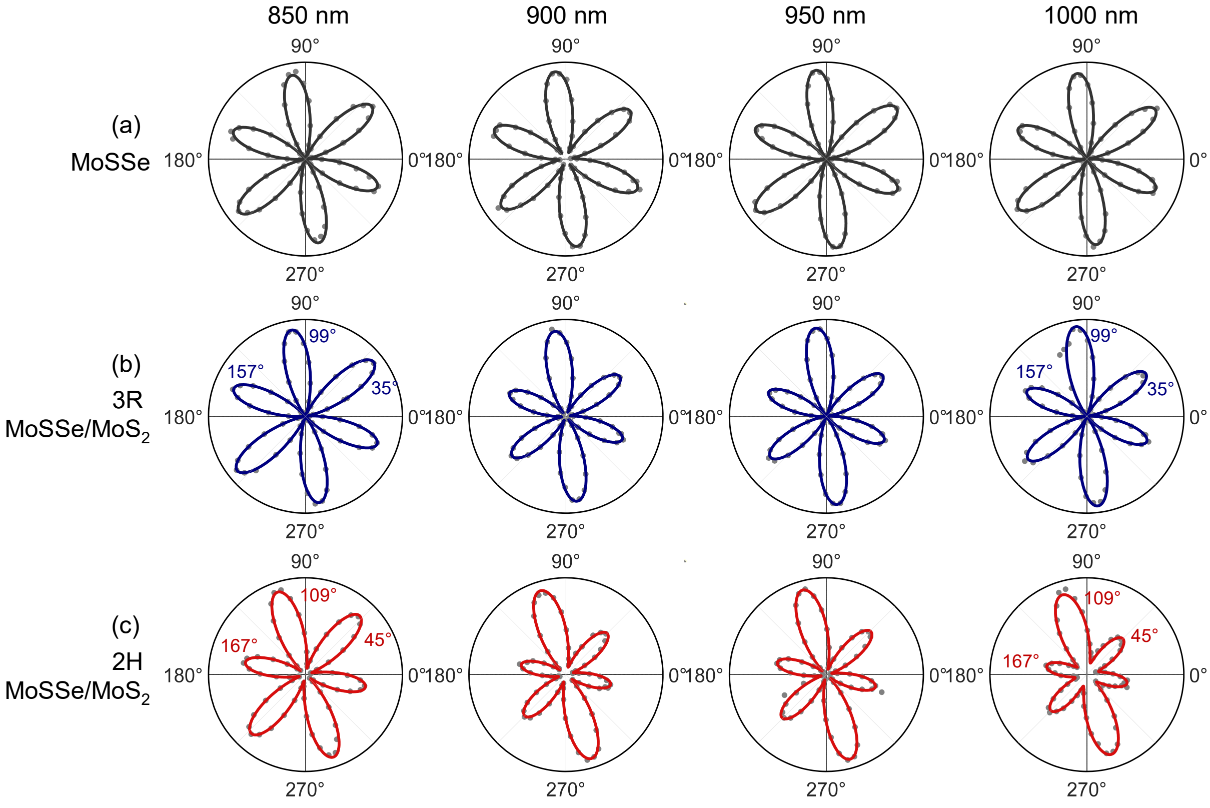

Figure 3. Wavelength-dependent polarization-resolved SHG intensity of (a) MoSSe, (b) 3R and (c) 2H MoSSe/MoS$_2$ heterostructures for incident wavelengths of 850 nm, 900 nm, 950 nm, and 1000 nm. The intensities are scaled to show anisotropy. The dots are the measured data, and the curves are the strained SHG fits, which will be discussed in the next section.

SHG Anisotropy Due to Strain

To quantify the deviation from group theory prediction, we define the intensity ratio ρ as the ratio of maximum to minimum intensities along the armchair directions, $\rho = I_{\parallel,x}^{\max}/I_{\parallel,x}^{\min}$ where x denotes the armchair direction. A larger intensity ratio reflects a stronger SHG anisotropy where the polarization dependence deviates from the six-fold symmetry. The SHG intensity ratio as a function of incident wavelength is summarized in Figure 4a-c. MoSSe shows a negligible intensity ratio of around 1.1 over the whole excitation range, while the intensity ratio of 3R MoSSe/MoS$_2$ significantly increases for excitation wavelengths beyond 875 nm and reaches a maximum of 1.44 at 925 nm and 975 nm excitations. Similarly, the 2H MoSSe/MoS$_2$ displays a large intensity ratio beyond 875 nm, with a maximum of $\rho = 1.73$ at 1000 nm excitations (Figure 4c).

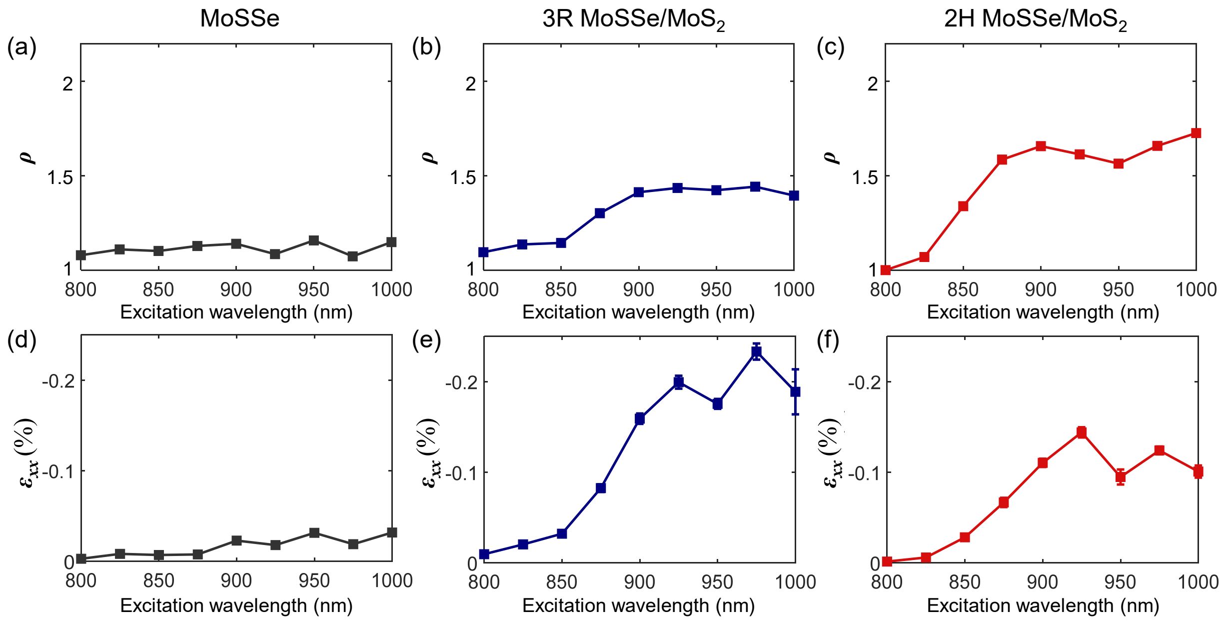

Figure 4. The fitted (a-c) intensity ratio and (d-f) fitted strain as a function of incident wavelength for MoSSe, 3R MoSSe/MoS$_2$, and 2H MoSSe/MoS$_2$ for $\varepsilon_{xx} = -\nu\varepsilon_{yy}$. The error bars in (d-f) are the standard deviations of the fitted parameters. Some error bars are too small to be seen.

The anisotropic SHG response can be potentially explained by the presence of strain, which can lift the degeneracy of optical responses. SHG intensity is related to the crystal structure through the second-order nonlinear susceptibility tensor $\chi_{ijk}^{(2)}$, where ijk denotes the polarization directions of the second harmonics and the fundamental excitations. The effect of strain can be described by a phenomenological photoelastic tensor p_{ijklm}, which represents how strain translates to optical changes. Then $\chi_{ijk}^{(2)}$ is written as $\chi_{ijk}^{(2)} = \chi_{ijk}^{(2,0)} + p_{ijklm}u_{lm}$, in which $\chi_{ijk}^{(2,0)}$ is the second-order susceptibility of unstrained systems and u_{lm} is the strain tensor, which can be converted into a principal strain basis with no shear component where $u_{lm} = \begin{pmatrix} \varepsilon_{xx} - \nu\varepsilon_{yy} & 0 \\ 0 & \varepsilon_{yy} - \nu\varepsilon_{xx} \end{pmatrix}$.[19] Here x and y denote the armchair and zigzag directions, respectively. $\nu = 0.29$ is the Poisson's ratio. Mennel et al.[19] have shown that the SHG intensity of a strained TMD monolayer can be described by

$$I_{\parallel} \propto \frac{1}{4}\left|A\cos(3\phi - 3\varphi_0) + B\cos(2\theta + \phi - \varphi_0)\right|^2 \qquad \text{Eq. 1}$$

with $A = (1-\nu)(p_1 + p_2)(\varepsilon_{xx} + \varepsilon_{yy}) + 2\chi_0$ and $B = (1+\nu)(p_1 - p_2)(\varepsilon_{xx} - \varepsilon_{yy})$, p_1 and p_2 are the photoelastic tensor elements, ε_{xx} and ε_{yy} are the principal strain elements, θ is the principal strain orientation, χ_0 is the SHG tensor element for unstrained TMDs. Eq. 1 suggests that the six-fold rotational symmetry of the SHG polar plots will be broken only when $\varepsilon_{xx} \neq \varepsilon_{yy}$.

In our measurement, χ_0 varies drastically with the incident wavelength. To rule out the influence of varied χ_0, we set χ_0 = 0.20, 0.45, 0.10 nm/V at 800 nm excitation for MoSSe, 3R and 2H heterostructures based on the first-principles calculations.[10] For longer wavelengths (λ), χ_0 is estimated using the measured SHG intensity, $\chi_0(\lambda) = \chi_0(800\ \mathrm{nm})\sqrt{\frac{I_{\parallel}(\lambda)}{I_{\parallel}(800\ \mathrm{nm})}}$. The corresponding χ_0 values used for each wavelength are provided in Table S1. We acknowledge that the phenomenological photoelastic tensor elements, p_1 and p_2, may also change upon different excitation wavelengths. However, according to Eq. 1, the parameters p_1, p_2 and the strain components ε_{xx}, ε_{yy} are interchangeable in the fitting process. As a result, fitting p_1, p_2 as a function of wavelength would show similar trends as fitting strain values ε_{xx}, ε_{yy}.

We fitted the SHG polar plots using Eq. 1, assuming biaxial deformation constrained by the Poisson effect ($\varepsilon_{yy} = -\nu\varepsilon_{xx}$). As shown in Figure 4d, the $|\varepsilon_{xx}|$ values of the MoSSe monolayer are significantly smaller than 0.1 % for all excitation wavelengths. While the MoSSe/MoS$_2$ heterostructures show an increased strain $|\varepsilon_{xx}|$ beyond 875 nm, reaching the values of $\varepsilon_{xx} = -0.23$ % for 3R at 975 nm and $\varepsilon_{xx} = -0.14$ % for 2H at 925 nm excitation (Figure 4e-f). The similar trends of the fitted strain and SHG intensity (Figure 2a-c and Figure 4d-f) suggest that optical resonance influences the nonlinear response of MoSSe/MoS$_2$ heterostructures. It is important to note that SHG anisotropy depends not only on strain but also on second-order susceptibility without strain, χ_0. For the same uniaxial compressive strain, a larger χ_0 leads to a smaller intensity ratio according to Eq.1 (Fig. S8), explaining why 3R MoSSe/MoS$_2$ exhibits a smaller intensity ratio despite having a higher fitted strain compared with 2H MoSSe/MoS$_2$.

Influence of Strain on $\chi^{(2)}$ by DFT Calculations

To confirm the strain effect on SHG anisotropy, we calculated the second-order susceptibility tensor under the strain of $\varepsilon_{xx} = -0.2$ % and $\varepsilon_{yy} = -\nu\varepsilon_{xx}$ (ν = 0.29) for 2H MoSSe/MoS$_2$ under different excitation wavelengths. In contrast to the calculations without strain (Figure 2d), the nonzero SHG tensor elements become nondegenerate when strain is considered, as shown in Figure 5a. Under the excitation wavelength with the maximum $|\chi^{(2)}|$, $\left|\chi^{(2)}_{yxy}\right|$ becomes slightly smaller than $\left|\chi^{(2)}_{xxx}\right|$ and $\left|\chi^{(2)}_{xyy}\right|$. In addition, the maximum $|\chi^{(2)}|$ shifts to shorter wavelengths as compared with no strain results due to an increase in transition energy at the Γ point by around 0.1 eV (Figure 5b), whereas the transition energies at the M point and K point show negligible changes, suggesting that the transition at the Γ point dominates the optical resonance effect.

In addition, the calculated band structures for 2H and 3R MoSSe/MoS$_2$ (Figure 5b and Fig. S9) reveal strong hybridization at the Γ point valence band with contributions from both MoS$_2$ and MoSSe. This hybridization highlights the role of stacking in enabling optical resonance, which leads to the observed wavelength-dependent SHG intensity. Since the intensity ratio is similarly affected by optical resonance as the SHG intensity, it is reasonable to assume that the anisotropy is related to the strong hybridization at the Γ point, which is absent in monolayer MoSSe, where no interlayer interactions exist.

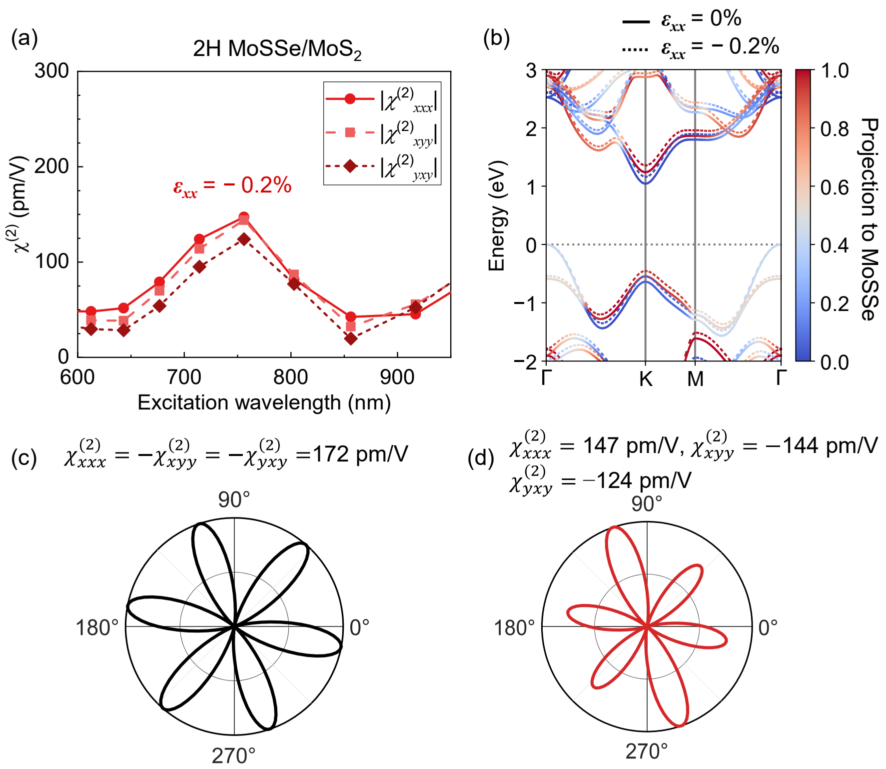

Figure 5. The calculated second-order susceptibility tensor with the strain of $\varepsilon_{xx} = -0.2$ % and $\varepsilon_{yy} = -\nu\varepsilon_{xx}$ (ν = 0.29) for 2H MoSSe/MoS$_2$. (a) The calculated SHG tensor elements with strain as a function of incident wavelength. (b) The calculated band structures with strain and without strain. (c-d) The simulated SHG polar plots based on group theory (c) without strain and (d) with strain (Details in Supplementary Note 1). φ_0 is set to be 109°.

We then simulated the SHG intensity polar plots using the calculated $|\chi^{(2)}|$ for both strained and unstrained 2H MoSSe/MoS$_2$ based on group theory. The polarization dependence of SHG intensity for the C$_{3v}$ point group can be represented by

$$I_{\parallel} = \left|\cos(\phi - \varphi_0)P_x(2\omega) + \sin(\phi - \varphi_0)P_y(2\omega)\right|^2 \qquad \text{Eq. 2}$$

where the second-order polarizations are denoted as $P_x(2\omega) = \chi^{(2)}_{xxx}E_0^2\cos(\phi - \varphi_0)^2 + \chi^{(2)}_{xyy}E_0^2\sin(\phi - \varphi_0)^2$ and $P_y(2\omega) = 2\chi^{(2)}_{yxy}E_0^2\cos(\phi - \varphi_0)\sin(\phi - \varphi_0)$. Without strain, the SHG intensity $I_{\parallel}$ shows a six-fold rotational symmetry (Figure 5c), while the strained case exhibits symmetry breaking (Figure 5d), consistent with the experimental results (Figure 3). This again confirms the presence of optically induced strain in Janus heterostructures.

Optically induced strain can result from several mechanisms, including photothermal expansion,[23] photostriction—which involves strain mediated by photoexcited charge carriers,[24-26] and optostriction, where the electromagnetic field directly interacts with the material's polarization response.[27] In our case, contributions from the first two mechanisms can be reasonably excluded. Photothermal expansion is typically isotropic in TMD materials and therefore cannot account for the anisotropic strain. On the other hand, photostriction generally requires above-bandgap excitation to generate carrier densities, particularly for ferroelectric or piezoelectric semiconductors. However, at longer excitation wavelengths, the generation of charge carriers in Janus heterostructures is minimal, as supported by the negligible photoluminescence intensity shown in Fig. S10. This indicates that photostriction is unlikely the dominant mechanism.

We therefore attribute the observed strain to optostriction,[27, 28] an optomechanical effect where the oscillating electromagnetic field of light couples directly to the dielectric response. Unlike photostriction, optostriction does not require charge carrier excitation and can occur under below-bandgap illumination. In this mechanism, the light-matter interaction results in elastic deformation as the system minimizes the Gibbs free energy in the presence of optical stress. While pristine MoSSe has an isotropic in-plane dielectric constant, anisotropic strain can emerge in MoSSe/MoS_2 heterostructures due to symmetry-breaking factors, such as intrinsic strain due to interfacial coupling or substrate interaction. Theoretical predictions for 1T' TMD monolayers[27] indicate that an excitation of 2×10^9 W/cm^2, which is comparable to that used in our SHG measurements (~10^9 W/cm^2, Methods), can induce a strain of 0.03% along the armchair direction through optostriction. This predicted strain lies within the range observed across different excitation wavelengths in our experiments (e.g., 0.02–0.23% for 3R MoSSe/MoS_2), supporting the plausibility of optically induced strain under our experimental conditions.

Strain Mediated by Interlayer Coupling

Here, we highlight the distinctive property of Janus materials that allows for the observation of optically induced strain, a phenomenon that has not been reported in conventional van der Waals heterostructures. Particularly, we discuss how the stacking configuration, i.e., 3R or 2H, affects the strain condition in Janus TMD heterostructures. In a MoSSe/MoS_2 heterostructure, the MoSSe layer exhibits intrinsic compressive strain because of lattice mismatch and Janus conversion that partly preserves the lattice. Raman spectroscopy further shows the difference in intrinsic strain between 2H and 3R stackings (Figure 6). The four MoSSe/MoS_2 heterostructures labeled S1-S4 display the A_1' mode of MoSSe and the E mode and A_1 mode of MoS_2 in the Raman spectrum (Figure 6b). The MoSSe A_1' mode has average frequencies of 292.8 cm^{-1} (S1) and 293.2 cm^{-1} (S2) for two 3R heterostructures, and 291.9 cm^{-1} (S3) and 292.2 cm^{-1} (S4) for two 2H heterostructures. The overall higher A_1' mode frequency of 3R MoSSe/MoS_2 compared with 2H MoSSe/MoS_2 by 1 cm^{-1} suggests a compressive strain of approximately 0.2 % present in the system,[29-31] which is on the same scale as the optically induced strain due to optostriction.

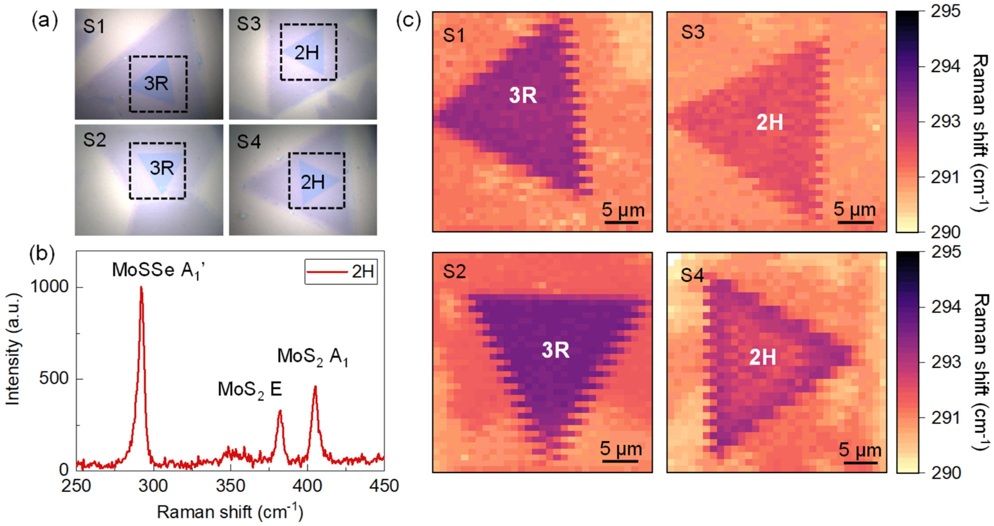

Figure 6. Raman spectroscopy of MoSSe/MoS_2 heterostructures. (a) Optical images of four MoSSe/MoS_2 with 3R or 2H stackings. (b) Raman spectra of 2H MoSSe/MoS_2. (c) Frequency maps of the A_1' mode in 3R and 2H MoSSe/MoS_2.

While doping and dielectric screening due to stacking can also affect phonon mode frequency,[32, 33] this effect is expected to show less significant difference between 2H and 3R than strain, as suggested by the calculated band structure for 3R and 2H heterostructures.[10] The larger intrinsic strain in 3R than 2H MoSSe/MoS_2 likely arises from the stronger interlayer coupling. Previous low-frequency Raman spectroscopy has shown that the in-plane interlayer force constant in 3R MoSSe/MoS_2 is ~6% higher than that of 2H MoSSe/MoS_2[7]. The stronger in-plane mechanical coupling due to stacking in 3R heterostructures is reflected by the larger shift of the E mode (in-plane) than the A_1 mode (out-of-plane) of MoS_2 when comparing 2H and 3R heterostructures (Fig. S11-12).

While it is uncertain whether the intrinsic strain is isotropic, it is plausible that the optically induced strain builds upon this pre-existing strain landscape, contributing to the observed SHG anisotropy. The presence of intrinsic strain also confirms that the heterostructure can sustain strain at this level without structural degradation. Our SHG measurement shows that 3R MoSSe/MoS_2 exhibits a higher optically induced strain than 2H MoSSe/MoS_2 (Figure 4e-f). This observation suggests that the stronger interlayer coupling in the 3R stacking may facilitate more effective strain transfer across the interface under optical excitation, thereby enhancing the optostrictive response compared with the 2H stacking. These results highlight the role of stacking-dependent interlayer coupling in enabling the optostriction effect in Janus heterostructures, a behavior absent in monolayer MoSSe and conventional TMD heterostructures.

In contrast to other 2D materials with strong SHG responses, such as PdPSe,[34] $NbOCl_2$,[35] or 3R MoS_2,[36] where SHG anisotropy arises from intrinsic crystal symmetry or in-plane displacement, the anisotropy in Janus MoSSe/MoS_2 heterostructures originates from optically induced anisotropic strain. This mechanism offers dynamic and controllable tunability, enabling sensitivity to subtle strain variations (~0.1%). Particularly, the intrinsic dipole moment of Janus MoSSe strengthens the interlayer coupling, resulting in efficient strain transfer across the interface. These findings suggest a complementary strategy to manipulate SHG response, offering potential routes to modulate anisotropy even in materials with inherently high nonlinear optical anisotropy.

Conclusions

In this work, we have demonstrated the optomechanical tuning of SHG anisotropy in MoSSe/MoS_2 heterostructures with 3R and 2H stackings. The polarization dependence of the SHG intensity deviates from the six-fold symmetry of the C_{3v} point group, particularly at longer excitation wavelengths. This anisotropy is attributed to strain-induced symmetry breaking within the heterostructures. The observed SHG anisotropy and intensity in MoSSe/MoS_2 both peak at incident wavelengths of 925 and 975 nm for 2H and 3R stackings, respectively, which corresponds to the resonance with transitions at the Γ point through second harmonics. These results suggest that optical resonance influenced by strong band hybridization plays a role in modulating optically induced strain, possibly through optostriction effects. Furthermore, the stronger photoinduced strain in 3R MoSSe/MoS_2 compared with 2H MoSSe/MoS_2 can be explained by the stronger interlayer coupling that affects both optically induced and inherent strain. These experimental results, supported by group theory analysis and first-principles calculations, underscore optostriction as the primary mechanism driving the anisotropic strain, especially in Janus-based heterostructures where symmetry breaking, electronic hybridization, and interlayer coupling play crucial roles. Our findings highlight the potential of SHG to investigate strain, stacking, and optical resonances, offering a valuable tool for exploring the nonlinear optical properties of van der Waals heterostructures.

Future studies can explore the dynamic modulation of strain in Janus heterostructures, enabling active control over their nonlinear optical properties and facilitating the extraction of photoelastic tensors. Moreover, the role of resonances in optostriction suggests opportunities for using optical excitation to manipulate nonlinear responses in these heterostructures. Further investigation using ultrafast spectroscopy could provide direct insights into the timescales and mechanisms of optomechanical effects. These prospective directions can deepen our understanding of strain-engineered functionalities and unlock opportunities for tunable nonlinear optical devices.

Methods

Janus MoSSe/MoS_2 synthesis:

The bilayer MoS_2 was synthesized using the method detailed in the reference.[37] The synthesis of Janus MoSSe/MoS_2 heterostructures was based on a previously reported atomic layer substitution (ALS) approach.[5] Chemical vapor deposition (CVD)-grown bilayer MoS_2 flakes with 3R and 2H stackings were used as the starting material. During the ALS conversion, the as-grown bilayer MoS_2 was placed in a horizontal tube reactor with an inductively coupled hydrogen plasma system. Selenium powder was positioned near the upstream edge of the plasma coil to enable the substitution reaction. The ALS reaction was conducted at room temperature, with a plasma power of 50 W and a reaction duration of 15 minutes.

SHG spectroscopy:

The SHG measurement was performed using a tunable laser (Coherent Chameleon Ultra II) with a repetition rate of 80 MHz and a pulse width of ~140 fs. The wavelength was tuned from 800 to 1000 nm with a 25 nm interval. A long-pass filter with a cut-off wavelength of 650 nm was used for incident wavelengths beyond 825 nm, and a long-pass filter with a cut-off wavelength of 900 nm was used for incident wavelengths beyond 925 nm. The laser was focused to a spot of 2 μm in diameter with a 100× objective. The powers used for incident wavelengths were 3.39, 1.15, 2.29, 0.98, 0.68, 0.74, 0.90, 0.45, and 0.51 mW, respectively. This corresponds to peak power densities of 19.3, 6.53, 13.0, 5.57, 3.87, 4.21, 5.11, 2.56, 2.90 $\times 10^9$ W/cm^2. Although the laser power densities we used vary slightly for each wavelength, the dependence of strain mostly follows the SHG intensity, suggesting a dominating effect of laser wavelength due to resonance. The incident laser and the signal were passed through a motorized achromatic half-wave plate, which changes the polarization direction of the laser. The second harmonic signals were collected onto a CCD camera using a spectrometer by setting the center wavelength to the corresponding wavelengths. For the polar plots, the measured SHG intensity was normalized by the incident powers. The details of fitting the polarization dependence can be found in Supplementary Note 2.

Raman and PL spectroscopy:

Raman and PL measurements were performed in a custom optical setup on the samples mounted in a Montana Cryostation S200. The sample was placed on piezoelectric-driven scanners in the cryostat to collect the corresponding intensity maps at room temperature. A 532 nm diode-pumped solid-state laser was used as the excitation source. The excitation beam was focused (< 1 μm diameter) onto the sample with a 100× objective (NA = 0.9). The emission or reflection signal from the sample is collected in back-scattering geometry and dispersed with Andor™ Kymera 328i spectrometer using a 1200 l/mm grating onto the detector (TE-cooled Andor™ Newton DU970P EMCCD). The laser excitation power on the sample used was ~ μW.

First-Principles Calculations:

The electronic band structures of MoSSe/MoS$_2$ with the 3R and 2H structures were performed by the density functional theory (DFT) method as implemented in Quantum ESPRESSO.[38, 39] The optimized norm-conserving Vanderbilt pseudopotentials[40] were used to describe the electron-ion interactions of the Mo, S, and Se atoms, and the exchange-correlation functional was treated within the generalized gradient approximation (GGA) of Perdew-Burke-Ernzerhof (PBE).[41] A plane-wave cutoff energy of 85 Ry was set. The Brillouin zone was sampled using a Monkhorst-Pack k-point mesh of $12 \times 12 \times 1$ and $24 \times 24 \times 1$ for the self-consistent and non-self-consistent calculations, respectively. To correct the energy band gap, the hybrid functional Heyd-Scuseria-Ernzerhof (HSE)[42] was used with a mixing parameter of 0.25 and a q-grid of $4 \times 4 \times 1$. After applying a strain of $\varepsilon_{xx} = -0.2\%$ in the x-direction and $\varepsilon_{yy} = 0.058\%$ in the y-direction, all structures were fully relaxed until the forces on each atom were less than 0.0001 Ry/a.u using the BFGS quasi-Newton algorithm.[39] The nonlocal van der Waals (vdW) correction was included in the relaxed calculations using the vdW-DF2 functional.[43] The second-order susceptibility tensor $\chi^{(2)}$ was calculated using the time-dependent DFT calculation as implemented in Yambo.[44] We noted that the calculated $\chi^{(2)}$ was scaled by the thickness of MoSSe/MoS_2 (1.3 nm).[10] All parameters were set to ensure the well-converged electronic structures and optical properties.

Author contributions

K.Z. and S.H. conceived the project. K.Z., M.D., E.B. performed the SHG measurements. M.D. performed the Raman measurements. K.Z. analyzed the experimental data and performed the group theory analysis. N.T.H. conducted the DFT calculations. T.Z. synthesized the Janus samples. R.S., J.K., A.R., S.H. supervised the project. K.Z. wrote the manuscript with input from all authors. All authors reviewed and approved the final manuscript.

Acknowledgment

K.Z. and S.H. acknowledge the support from the National Science Foundation (NSF) (grant nos. ECCS-2246564 and ECCS-1943895) and Air Force Office of Scientific Research (AFOSR) under grant FA9550-22-1-0408. S.H. also acknowledges the support from the Welch Foundation (award no. C-2144). T.Z. and J.K. acknowledge the support from the U.S. Department of Energy, Office of Science, Basic Energy Sciences, under award number DE-SC0020042 and the Air Force Office of Scientific Research under award number FA2386-24-1-4049. Any opinions, finding, and conclusions or recommendations expressed in this material are those of the author(s) and do not necessarily reflect the views of the United States Air Force. R.S. acknowledges the Yushan Fellow Program by the Ministry of Education (MOE), Taiwan. We acknowledge Dr. Xufan Li for help with the MoS_2 synthesis. SHG Microscopy and data analysis at the Molecular Foundry were supported by the U.S. Department of Energy Office of Science under the Microelectronics Science Research Center (Nanoscale Hybrids: A New Paradigm for Energy-efficient Optoelectronics), Contract DE-AC02-05-CH11231.

Supporting Information

Supporting Information includes group theory analysis and fitting results of the polarization-resolved second harmonic generation (SHG), schematic illustration of the synthesis, first-principles calculations and experimental SHG spectra of 3R MoSSe/MoS_2, the fitted Raman frequencies of 3R and 2H MoSSe/MoS_2. The Supporting Information is available online.

References

1. Du, L.; Hasan, T.; Castellanos-Gomez, A.; Liu, G.-B.; Yao, Y.; Lau, C. N.; Sun, Z. Engineering Symmetry Breaking in 2D Layered Materials. *Nature Reviews Physics* **2021**, *3*, 193—206.

2. Lu, A.-Y.; Zhu, H.; Xiao, J.; Chuu, C.-P.; Han, Y.; Chiu, M.-H.; Cheng, C.-C.; Yang, C.-W.; Wei, K.-H.; Yang, Y.; Wang, Y.; Sokaras, D.; Nordlund, D.; Yang, P.; Muller, D. A.; Chou, M.-Y.; Zhang, X.; Li, L.-J. Janus Monolayers of Transition Metal Dichalcogenides. *Nature Nanotechnology* **2017**, *12*, 744—749.
3. Zhang, J.; Jia, S.; Kholmanov, I.; Dong, L.; Er, D.; Chen, W.; Guo, H.; Jin, Z.; Shenoy, V. B.; Shi, L.; Lou, J. Janus Monolayer Transition-Metal Dichalcogenides. *ACS Nano* **2017**, *11*, 8192—8198.
4. Lin, Y.-C.; Liu, C.; Yu, Y.; Zarkadoula, E.; Yoon, M.; Puretzky, A. A.; Liang, L.; Kong, X.; Gu, Y.; Strasser, A.; Meyer, H. M., III; Lorenz, M.; Chisholm, M. F.; Ivanov, I. N.; Rouleau, C. M.; Duscher, G.; Xiao, K.; Geohegan, D. B. Low Energy Implantation into Transition-Metal Dichalcogenide Monolayers to Form Janus Structures. *ACS Nano* **2020**, *14*, 3896—3906.
5. Guo, Y.; Lin, Y.; Xie, K.; Yuan, B.; Zhu, J.; Shen, P.-C.; Lu, A.-Y.; Su, C.; Shi, E.; Zhang, K.; HuangFu, C.; Xu, H.; Cai, Z.; Park, J.-H.; Ji, Q.; Wang, J.; Dai, X.; Tian, X.; Huang, S.; Dou, L.; et al. Designing Artificial Two-Dimensional Landscapes via Atomic-Layer Substitution. *Proceedings of the National Academy of Sciences* **2021**, *118*, e2106124118.
6. Dong, L.; Lou, J.; Shenoy, V. B. Large In-Plane and Vertical Piezoelectricity in Janus Transition Metal Dichalchogenides. *ACS Nano* **2017**, *11*, 8242—8248.
7. Zhang, K.; Guo, Y.; Ji, Q.; Lu, A.-Y.; Su, C.; Wang, H.; Puretzky, A. A.; Geohegan, D. B.; Qian, X.; Fang, S.; Kaxiras, E.; Kong, J.; Huang, S. Enhancement of van der Waals Interlayer Coupling through Polar Janus MoSSe. *Journal of the American Chemical Society* **2020**, *142*, 17499—17507.
8. Zhang, K.; Guo, Y.; Larson, D. T.; Zhu, Z.; Fang, S.; Kaxiras, E.; Kong, J.; Huang, S. Spectroscopic Signatures of Interlayer Coupling in Janus MoSSe/MoS_2 Heterostructures. *ACS Nano* **2021**, *15*, 14394—14403.
9. Shi, J.; Xu, H.; Heide, C.; HuangFu, C.; Xia, C.; de Quesada, F.; Shen, H.; Zhang, T.; Yu, L.; Johnson, A.; Liu, F.; Shi, E.; Jiao, L.; Heinz, T.; Ghimire, S.; Li, J.; Kong, J.; Guo, Y.; Lindenberg, A. M. Giant Room-Temperature Nonlinearities in a Monolayer Janus Topological Semiconductor. *Nature Communications* **2023**, *14*, 4953.
10. Hung, N. T.; Zhang, K.; Van Thanh, V.; Guo, Y.; Puretzky, A. A.; Geohegan, D. B.; Kong, J.; Huang, S.; Saito, R. Nonlinear Optical Responses of Janus MoSSe/MoS_2 Heterobilayers Optimized by Stacking Order and Strain. *ACS Nano* **2023**, *17*, 19877—19886.
11. Petrić, M. M.; Villafañe, V.; Herrmann, P.; Ben Mhenni, A.; Qin, Y.; Sayyad, Y.; Shen, Y.; Tongay, S.; Müller, K.; Soavi, G.; Finley, J. J.; Barbone, M. Nonlinear Dispersion Relation and Out-of-Plane Second Harmonic Generation in MoSSe and WSSe Janus Monolayers. **2023**, *11*, 2300958.
12. Shree, S.; Lagarde, D.; Lombez, L.; Robert, C.; Balocchi, A.; Watanabe, K.; Taniguchi, T.; Marie, X.; Gerber, I. C.; Glazov, M. M.; Golub, L. E.; Urbaszek, B.; Paradisanos, I. Interlayer Exciton Mediated Second Harmonic Generation in Bilayer MoS_2. *Nature Communications* **2021**, *12*, 6894.
13. Kim, W.; Jeong, G.; Oh, J.; Kim, J.; Watanabe, K.; Taniguchi, T.; Ryu, S. Exciton-Sensitized Second-Harmonic Generation in 2D Heterostructures. *ACS Nano* **2023**, *17*, 20580—20588.
14. Le, C. T.; Clark, D. J.; Ullah, F.; Jang, J. I.; Senthilkumar, V.; Sim, Y.; Seong, M.-J.; Chung, K.-H.; Kim, J. W.; Park, S.; Rhim, S. H.; Kim, G.; Kim, Y. S. Impact of Selenium Doping on Resonant Second-Harmonic Generation in Monolayer MoS_2. *ACS Photonics* **2017**, *4*, 38—44.

15. Clark, D. J.; Senthilkumar, V.; Le, C. T.; Weerawarne, D. L.; Shim, B.; Jang, J. I.; Shim, J. H.; Cho, J.; Sim, Y.; Seong, M. J.; Rhim, S. H.; Freeman, A. J.; Chung, K. H.; Kim, Y. S. Strong Optical Nonlinearity of CVD-Grown MoS_2 Monolayer as Probed by Wavelength-Dependent Second-Harmonic Generation. *Physical Review B* **2014**, *90*, 121409.
16. Hsu, W.-T.; Zhao, Z.-A.; Li, L.-J.; Chen, C.-H.; Chiu, M.-H.; Chang, P.-S.; Chou, Y.-C.; Chang, W.-H. Second Harmonic Generation from Artificially Stacked Transition Metal Dichalcogenide Twisted Bilayers. *ACS Nano* **2014**, *8*, 2951—2958.
17. Mennel, L.; Paur, M.; Mueller, T. Second Harmonic Generation in Strained Transition Metal Dichalcogenide Monolayers: MoS_2, $MoSe_2$, WS_2, and WSe_2. *APL Photonics* **2018**, *4*, 034404.
18. Khan, A. R.; Liu, B.; Lü, T.; Zhang, L.; Sharma, A.; Zhu, Y.; Ma, W.; Lu, Y. Direct Measurement of Folding Angle and Strain Vector in Atomically Thin WS_2 Using Second-Harmonic Generation. *ACS Nano* **2020**, *14*, 15806—15815.
19. Mennel, L.; Furchi, M. M.; Wachter, S.; Paur, M.; Polyushkin, D. K.; Mueller, T. Optical Imaging of Strain in Two-Dimensional Crystals. *Nature Communications* **2018**, *9*, 516.
20. Zheng, X.; Zhang, K.; Zhao, X.; Zhou, J.; Shen, H.; Kong, J.; Guo, Y. Achieving High-Yield Conversion of Janus Transition Metal Dichalcogenides on Diverse Substrates. *ACS Nano* **2025**, *19*, 20744—20752.
21. Zheng, T.; Lin, Y.-C.; Yu, Y.; Valencia-Acuna, P.; Puretzky, A. A.; Torsi, R.; Liu, C.; Ivanov, I. N.; Duscher, G.; Geohegan, D. B.; Ni, Z.; Xiao, K.; Zhao, H. Excitonic Dynamics in Janus MoSSe and WSSe Monolayers. *Nano Letters* **2021**, *21*, 931—937.
22. Beach, K.; Lucking, M. C.; Terrones, H. Strain Dependence of Second Harmonic Generation in Transition Metal Dichalcogenide Monolayers and the Fine Structure of the C Exciton. *Physical Review B* **2020**, *101*, 155431.
23. Zhang, L.; Lu, Z.; Song, Y.; Zhao, L.; Bhatia, B.; Bagnall, K. R.; Wang, E. N. Thermal Expansion Coefficient of Monolayer Molybdenum Disulfide Using Micro-Raman Spectroscopy. *Nano Letters* **2019**, *19*, 4745—4751.
24. Lejman, M.; Vaudel, G.; Infante, I. C.; Gemeiner, P.; Gusev, V. E.; Dkhil, B.; Ruello, P. Giant Ultrafast Photo-Induced Shear Strain in Ferroelectric $BiFeO_3$. *Nature Communications* **2014**, *5*, 4301.
25. Matzen, S.; Guillemot, L.; Maroutian, T.; Patel, S. K. K.; Wen, H.; DiChiara, A. D.; Agnus, G.; Shpyrko, O. G.; Fullerton, E. E.; Ravelosona, D.; Lecoeur, P.; Kukreja, R. Tuning Ultrafast Photoinduced Strain in Ferroelectric-Based Devices. *Advanced Electronic Materials* **2019**, *5*, 1800709.
26. Wen, H.; Chen, P.; Cosgriff, M. P.; Walko, D. A.; Lee, J. H.; Adamo, C.; Schaller, R. D.; Ihlefeld, J. F.; Dufresne, E. M.; Schlom, D. G.; Evans, P. G.; Freeland, J. W.; Li, Y. Electronic Origin of Ultrafast Photoinduced Strain in $BiFeO_3$. *Physical Review Letters* **2013**, *110*, 037601.
27. Zhou, J.; Mao, S.; Zhang, S. Noncontacting Optostriction Driven Anisotropic and Inhomogeneous Strain in Two-Dimensional Materials. *Physical Review Research* **2020**, *2*, 022059.
28. Zhou, J. Tailoring geometric phases of two-dimensional functional materials under light: a brief review. *International Journal of Smart and Nano Materials* **2020**, *11*, 191-206.
29. Rice, C.; Young, R. J.; Zan, R.; Bangert, U.; Wolverson, D.; Georgiou, T.; Jalil, R.; Novoselov, K. S. Raman-Scattering Measurements and First-Principles Calculations of Strain-Induced Phonon Shifts in Monolayer MoS_2. *Physical Review B* **2013**, *87*, 081307.

30. Conley, H. J.; Wang, B.; Ziegler, J. I.; Haglund, R. F., Jr.; Pantelides, S. T.; Bolotin, K. I. Bandgap Engineering of Strained Monolayer and Bilayer MoS_2. *Nano Letters* **2013**, *13*, 3626—3630.
31. Lee, J.-U.; Woo, S.; Park, J.; Park, H. C.; Son, Y.-W.; Cheong, H. Strain-Shear Coupling in Bilayer MoS_2. *Nature Communications* **2017**, *8*, 1370.
32. Ciampalini, G.; Fabbri, F.; Menichetti, G.; Buoni, L.; Pace, S.; Mišeikis, V.; Pitanti, A.; Pisignano, D.; Coletti, C.; Tredicucci, A.; Roddaro, S. Unexpected Electron Transport Suppression in a Heterostructured Graphene–MoS_2 Multiple Field-Effect Transistor Architecture. *ACS Nano* **2022**, *16*, 1291—1300.
33. Kukucska, G.; Koltai, J. Theoretical Investigation of Strain and Doping on the Raman Spectra of Monolayer MoS_2. *physica status solidi (b)* **2017**, *254*, 1700184.
34. Zhu, S.; Duan, R.; Xu, X.; Sun, F.; Chen, W.; Wang, F.; Li, S.; Ye, M.; Zhou, X.; Cheng, J.; Wu, Y.; Liang, H.; Kono, J.; Li, X.; Liu, Z.; Wang, Q. J. Strong nonlinear optical processes with extraordinary polarization anisotropy in inversion-symmetry broken two-dimensional PdPSe. *Light: Science & Applications* **2024**, *13*, 119.
35. Abdelwahab, I.; Tilmann, B.; Zhao, X.; Verzhbitskiy, I.; Berté, R.; Eda, G.; Wilson, W. L.; Grinblat, G.; de S. Menezes, L.; Loh, K. P.; Maier, S. A. Highly efficient sum-frequency generation in niobium oxydichloride $NbOCl_2$ nanosheets. *Advanced Optical Materials* **2023**, *11*, 2202833.
36. Shi, J.; Yu, P.; Liu, F.; He, P.; Wang, R.; Qin, L.; Zhou, J.; Li, X.; Zhou, J.; Sui, X.; Zhang, S.; Zhang, Y.; Zhang, Q.; Sum, T. C.; Qiu, X.; Liu, Z.; Liu, X. 3R MoS_2 with broken inversion symmetry: a promising ultrathin nonlinear optical device. **2017**, *29*, 1701486.
37. Li, X.; Kahn, E.; Chen, G.; Sang, X.; Lei, J.; Passarello, D.; Oyedele, A. D.; Zakhidov, D.; Chen, K.-W.; Chen, Y.-X.; Hsieh, S.-H.; Fujisawa, K.; Unocic, R. R.; Xiao, K.; Salleo, A.; Toney, M. F.; Chen, C.-H.; Kaxiras, E.; Terrones, M.; Yakobson, B. I.; et al. Surfactant-Mediated Growth and Patterning of Atomically Thin Transition Metal Dichalcogenides. *ACS Nano* **2020**, *14*, 6570—6581.
38. Giannozzi, P.; Baroni, S.; Bonini, N.; Calandra, M.; Car, R.; Cavazzoni, C.; Ceresoli, D.; Chiarotti, G. L.; Cococcioni, M.; Dabo, I.; Dal Corso, A.; de Gironcoli, S.; Fabris, S.; Fratesi, G.; Gebauer, R.; Gerstmann, U.; Gougoussis, C.; Kokalj, A.; Lazzeri, M.; Martin-Samos, L.; et al. QUANTUM ESPRESSO: A Modular and Open-Source Software Project for Quantum Simulations of Materials. *J Phys Condens Matter* **2009**, *21*, 395502.
39. Hung, N. T.; Nugraha, A. R.; Saito, R., *Quantum ESPRESSO Course for Solid-State Physics*. Jenny Stanford Publishing: 2022.
40. Hamann, D. Optimized Norm-Conserving Vanderbilt Pseudopotentials. *Physical Review B* **2013**, *88*, 085117.
41. Perdew, J. P.; Burke, K.; Ernzerhof, M. J. P. r. l. Generalized Gradient Approximation Made Simple. *Physical Review Letters* **1996**, *77*, 3865.
42. Heyd, J.; Scuseria, G. E.; Ernzerhof, M. Hybrid Functionals Based on a Screened Coulomb Potential. *The Journal of Chemical Physics* **2003**, *118*, 8207—8215.
43. Lee, K.; Murray, É. D.; Kong, L.; Lundqvist, B. I.; Langreth, D. C. Higher-Accuracy van der Waals Density Functional. *Physical Review B* **2010**, *82*, 081101.
44. Marini, A.; Hogan, C.; Grüning, M.; Varsano, D. Yambo: An *ab initio* Tool for Excited State Calculations. *Computer Physics Communications* **2009**, *180*, 1392—1403.

TOC

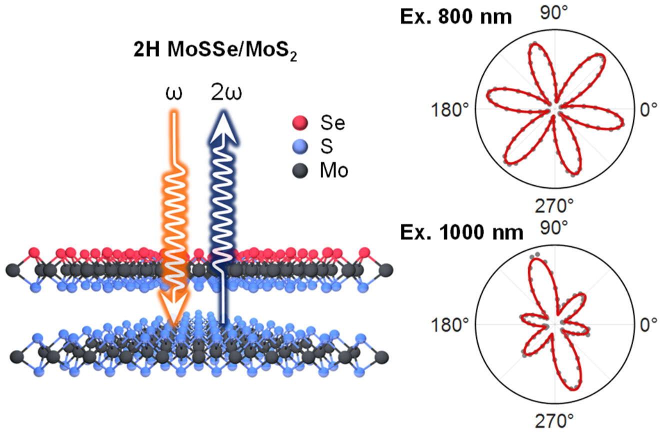
2H MoSSe/MoS$_2$
ω
2ω
Se
S
Mo
Ex. 800 nm
90°
180°
0°
270°
Ex. 1000 nm
90°
180°
0°
270°